JOURNAL OF APPLIED CRYSTALLOGRAPHY
ISSN 1600-5767

Construction of a quartz spherical analyzer: application to high-resolution analysis of the Ni *Kα* emission spectrum

Marcelo Goncalves Honnicke,[a]* Leonardo M. Bianco,[b] Sergio A. Ceppi,[b,c] Cesar Cusatis,[d] XianRong Huang,[e] Yong Q. Cai[f] and Guillermo E. Stutz[b,c]*

[a]Instituto de Ciencias da Vida e da Natureza, Universidade Federal da Integracao Latino-Americana, 2044, Foz do Iguacu, Parana 85867-970, Brazil, [b]Facultad de Matemática, Astronomía y Física, Universidad Nacional de Córdoba, 5000, Córdoba, Argentina, [c]Instituto de Física E. Gaviola, CONICET-UNC, 5000, Córdoba, Argentina, [d]Departamento de Fisica, Universidade Federal do Parana, 19091, Curitiba, Parana 81531-980, Brazil, [e]X-ray Science Division, Argonne National Laboratory, 9700 South Cass Avenue, Argonne, IL, USA, and [f]National Synchrotron Light Source II, Brookhaven National Laboratory, Upton, NY 11973, USA. *Correspondence e-mail: marcelo.honnicke@unila.edu.br, stutz@famaf.unc.edu.br

Received 21 February 2016
Accepted 30 June 2016

Edited by V. Holý, Charles University, Prague, Czech Republic

Keywords: spherical analyzers; X-ray emission spectroscopy; inelastic X-ray scattering; X-ray optics; quartz crystals.

The construction and characterization of a focusing X-ray spherical analyzer based on α-quartz $4\bar{4}04$ are presented. The performance of the analyzer was demonstrated by applying it to a high-resolution X-ray spectroscopy study of the $K\alpha_{1,2}$ emission spectrum of Ni. An analytical representation based on physical grounds was assumed to model the shape of the X-ray emission lines. Satellite structures assigned to $3d$ spectator hole transitions were resolved and determined as well as their relative contribution to the emission spectrum. The present results on $1s^{-1}3d^{-1}$ shake probabilities support a recently proposed calculation framework based on a multi-configuration atomic model.

1. Introduction

X-ray spectroscopy studies involving the spectral analysis of inelastically scattered X-rays (inelastic X-ray scattering spectroscopy, IXS) or characteristic X-ray emission lines (X-ray emission spectroscopy, XES) demand that crystal analyzers provide both high energy resolution and high collection efficiency. Such requirements are met by spherically bent analyzers, as firstly shown in IXS applications (Schülke & Nagasawa, 1984). These devices are built to work, in the majority of cases, close to the back-diffraction geometry, such that they present high energy resolution while maintaining a reasonable solid angle of collection (realized by the spherical focusing geometry). This allows collection of X-ray spectroscopy data with adequate signal-to-noise ratios (Cai, 2004; Hill *et al.*, 2007; Mortensen *et al.*, 2013), even for low-energy synchrotron sources (Tirao *et al.*, 2004). More recently, the use of multiple spherical crystals, for further increasing the collection solid angle, has also been implemented (Fister *et al.*, 2006; Verbeni *et al.*, 2009; Sokaras *et al.*, 2013; Ishikawa *et al.*, 2015), especially for inelastic X-ray scattering purposes. Depending on the type of interactions to be explored using X-ray spectrometers, the required energy resolution ranges from a few eV to sub meV. Such requirements are the basis for different construction procedures of spherical analyzers (Verbeni *et al.*, 2005). The fabrication of spherical analyzers involves, in most cases, the use of high-quality Si or Ge single crystals. With the availability of other high-quality single crystals, such as α-Al_2O_3 (sapphire), $LiNbO_3$, SiC, GaN and

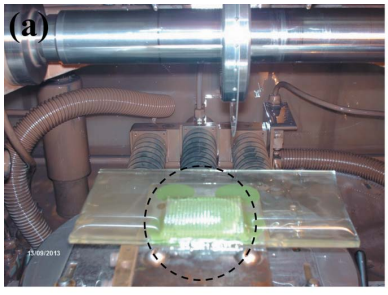

α-SiO_2 (quartz), new opportunities for X-ray optics have arisen. In fact, sapphire has been used for making IXS spherical analyzers (Yavaş *et al.*, 2007; Sergueev *et al.*, 2011). Quartz and $LiNbO_3$ spherical analyzers have also been proposed for IXS studies, since they offer high energy resolution at lower photon energies (Sutter *et al.*, 2005, 2006; Gog *et al.*, 2013; Hönnicke *et al.*, 2013; Ketenoglu *et al.*, 2015). One of the main motivations for the development of quartz-based spherical analyzers is that they offer a large choice of reflections within a given photon energy interval owing to the lower crystal symmetry with respect to silicon or germanium. The application of bent quartz crystals has also been considered in other fields, such as X-ray microscopy and backlighting imaging techniques using plasma sources (Sinars *et al.*, 2003). In this field, tests of backlighting systems using the SiHeα emission line along with a bent quartz $10\bar{1}1$ crystal analyzer of a 0.25 m curvature radius have already been performed on a Z-machine (Sinars *et al.*, 2003).

X-ray spectral analysis using crystals in nearly back-diffraction geometry imposes the matching relationship $\lambda \simeq 2d_{hkl}$ between the X-ray wavelength (λ) and the diffracting lattice plane spacing (d_{hkl}). In non-resonant IXS, since the energy-loss spectrum is measured, there is no additional restriction on the analyzed energy other than those related to sample absorption and energy resolution (Schülke, 1991). On the other hand, for XES and resonant IXS, since the spectral distribution is composed of discrete wavelengths, different diffracting planes and crystals having different lattice parameters are required to cover a wide range of particular experimental situations (a number of spectral lines emitted by a specific element).

Measurements of emission spectra with high energy resolution, *i.e.* with a spectrometer energy bandwidth narrower than the natural line width, open possibilities of resolving satellite structures as well as analyzing spectral line shapes with high accuracy. This makes it feasible to study the complexity of the emission spectrum structure of open 3*d* shell atoms. Here a comprehensive understanding of the emission spectra structures and an accurate modeling of the emission lines are of fundamental importance in many areas, ranging from chemical physics, through the study of chemical environment dependent features of the valence-to-core emission spectrum (Torres Deluigi *et al.*, 2014), to plasma physics and astrophysics (Palmeri *et al.*, 2008). Also, in fundamental atomic physics, much progress in *ab initio* reconstruction of atomic spectra and evaluation of spectral parameters has been made (Chantler *et al.*, 2009, 2010, 2013; Lowe *et al.*, 2010). These theoretical developments have increased further demands on energy resolution and accuracy of experimental data for future XES experiments.

In this paper, the fabrication procedure and the characterization of an α-quartz $44\bar{0}4$ spherical analyzer will be presented, followed by the application of the spherical analyzer to a high-resolution measurement of the Ni $K\alpha_{1,2}$ emission spectrum. Finally, results obtained for several spectral parameters will be discussed and compared with other experimental work and theoretical results.

2. Spherical quartz analyzer

2.1. Fabrication

The synthetic α-quartz crystal used to fabricate our spherical analyzer is a grade-*A* crystal (in terms of the quality factor *Q*) acquired from TEW Japan. It was a single block of 240 × 79 × 40 mm and has been characterized to have very good crystalline quality with variations in the lattice parameter being $\Delta d/d \simeq 5 \times 10^{-7}$ (Hönnicke *et al.*, 2013). We oriented the crystal, from which we cut a number of square $(1\bar{1}01)$ wafers [36 mm (horizontally) × 40 mm (vertically) × 3 mm thick]. After lapping and etching, each wafer was then diced into small blocks of 1.5 × 1.5 × 2.5 mm (groove depth) giving a total of 360 small crystal blocks (Fig. 1). The diced wafers were subsequently etched again in a 50% HF solution for 10 min, then glued on a spherical concave substrate, which was made of tempered glass with a curvature radius of 1 m.

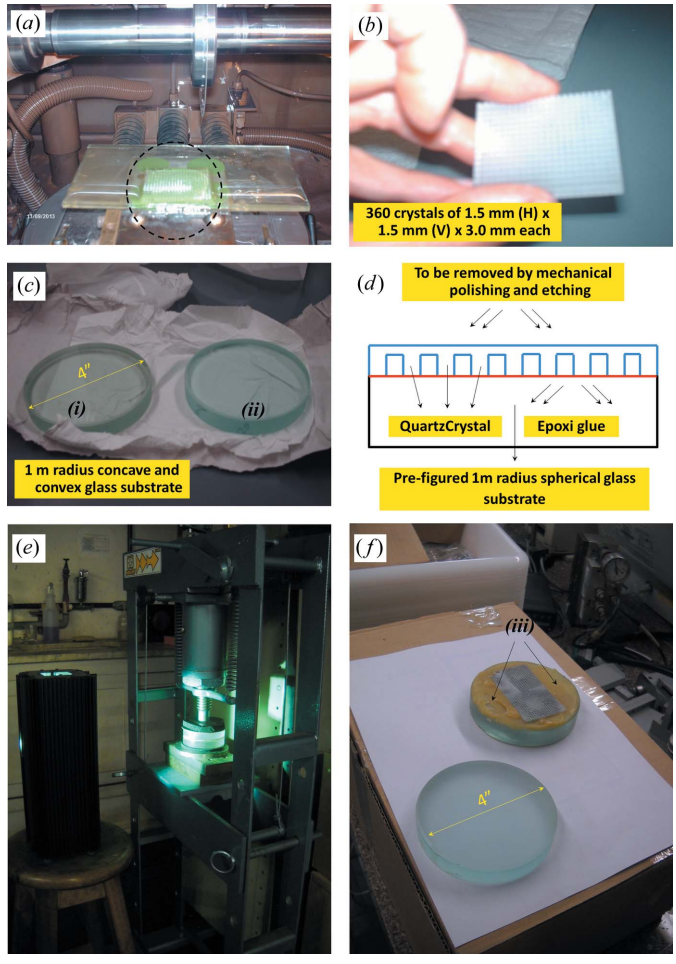

Figure 1
Fabrication steps of the spherical quartz analyzer. (*a*) Wafer dicing process. The square-shaped wafer is shown inside the dashed black circle. (*b*) The wafer after dicing and etching with 50% HF solution for 10 min. (*c*) The 1 m radius glass spherical substrates prior to quartz wafer bonding: (i) convex and (ii) concave substrate. (*d*) Schematic representation of the bonding process. (*e*) Bonding and cure process under pressure. (*f*) The quartz spherical analyzer after the final lapping/etching procedure, where the entire glass substrate is embedded in beeswax (iii) to avoid HF substrate damage.

For gluing, a standard procedure was adopted, *i.e.* the wafers were glued with the small crystals in contact with the substrate and the solid thin wafer part (0.5 mm thick) was left on the top, to be removed later by polishing and further etching after the gluing process. The gluing process was carried out by applying pressure (1 t cm^{-2} for 24 h; 1 t = 1000 kg) on the wafer against the substrate and under UV radiation exposure. The purpose is to ensure that each small crystal follows the substrate radius. The UV radiation is required for the cure of the epoxy glue (LOCTITE LI 1210). The bent quartz crystal was lapped again with SiC abrasive powder and a convex glass substrate to remove the thin bent crystal layer. However, during the lapping process we realized that the glue would not be strong enough to hold the small crystal blocks once the thin crystal layer was removed. Therefore, we decided to lap the bent thin crystal layer to make it as thin as possible. Following that, the concave glass substrate was covered by beeswax in order to protect it from the HF solution in the final etching procedure of the spherical quartz analyzer.

During the final etching, even after leaving the crystal for 2 h in a 50% HF solution, there was no significant layer removal. Then, as mentioned above, since the glue was not strong enough to hold the small crystal blocks, we decided to leave the crystal as it was. We aim, for future mounting, to glue the diced quartz surface onto an Si wafer, dice the opposite quartz thin layer again and then glue, by sandwiching the Si wafer and the diced quartz, into the tempered glass substrate. This procedure is similar to that described by Ketenoglu *et al.* (2015).

2.2. Characterization: X-ray topography

After the fabrication processes, we characterized the spherical quartz analyzer using a modified Berg–Barrett X-ray topography (Berg, 1931; Barrett, 1945; Tanner, 1976).

X-ray topography is an imaging technique used to detect crystal defects (inclusions, dislocations, impurity distributions *etc*.). A detailed description of the technique is beyond the scope of this work; however, clever reviews on the different X-ray topography methods are given by Härtwig (1999) and Authier (2001). On the basis on these works, in brief, the technique can be classified into different methods: (i) extended-beam methods and (ii) the limited-beam method. Included in the extended-beam methods are the integrated wave topography techniques (Berg–Barrett topography, white-beam topography and Lang topography) and the double-crystal topography technique. The limited-beam method is the section topography technique. The Berg–Barrett topography setup (Berg, 1931; Barrett, 1945; Tanner, 1976; Authier, 2001) is based on the imaging acquired from diffraction of a particular set of lattice planes with a divergence/chromaticity coming from an extended source (which can be the characteristic line in a conventional X-ray source or the spectral width of a monochromator in synchrotrons). The white-beam topography setup is basically the same as that used in the Laue method (Culity & Stock, 2014). The technique was first used with conventional X-ray sources by Ramachandran (1944); it was later carried out with a synchrotron source (Tuomi *et al.*, 1974), where it has since been extensively used (Dudley *et al.*, 1995; Barrett *et al.*, 1995; Härtwig, 1999). The Lang topography setup (Lang, 1959; Tanner, 1976; Härtwig, 1999) is based on scanning the crystal (which is diffracting at a particular set of lattice planes) across a collimated X-ray beam. As in the Berg–Barrett topography, the divergence/chromaticity of the extended source can be the characteristic line in a conventional X-ray source or the spectral width of a monochromator in a synchrotron source. In the double-crystal topography (Bond & Andrus, 1952), the first crystal is, often, an asymmetrically cut monochromator. The second crystal is the sample under analysis. When the crystals are used in the non-dispersive arrangement (+,−) (Dumond, 1937), the setup is a prototype of plane-wave topography. More recently, Lübbert *et al.* (2000, 2005) used the double-crystal topography setup by taking several topography images with modern pixel detectors, for different semiconductor analysis. Lastly, the section topography technique (Tanner, 1976; Härtwig, 1999; Authier, 2001) is based on the restriction to a few micrometres of the incoming beam width (perpendicular to the scattering plane). Then one can obtain, even from a perfect crystal, an inhomogeneous topography image.

As mentioned before, precise characterization of the original quartz crystal has been presented elsewhere (Hönnicke *et al.*, 2013), which shows $\Delta d/d \simeq 5 \times 10^{-7}$. Previous work, also on the top-grade quartz single crystal provided by TEW Japan, showed results with $\Delta d/d$ ranging from 3×10^{-7} to 5×10^{-7} (Sutter *et al.*, 2006). Here, the main goal of further characterization is to understand approximately the misorientations ($\Delta\theta$) of the crystal blocks on the concave spherical substrates as well as the bent strain level ($\Delta d/d$) due to the remaining thin continuous crystal layer. We emphasize here that we only wish to gain an approximate idea about the misorientations and the bent strain level; the geometry is complex and it is not possible here to carry out a more quantitative analysis.

In the modified Berg–Barrett X-ray topography setup, based on grazing-incidence asymmetric diffraction (Fig. 2), the resolution ($\Delta d/d$ and misorientations $\Delta\theta$) is dominated by the natural line width of the Cu $K\beta$ X-ray emission line (∼5.84 eV) and the asymmetry factor (b). The asymmetry factor (b) is the inverse of the lateral X-ray beam magnification ($b = -1/m$; m stands for magnification) provided by asymmetric diffraction in perfect single crystals (Pinsker, 1978). The minus sign is applied only for the Bragg case, *i.e.* the diffraction happens on the same crystal side as is hit by the incoming X-ray beam. The smaller the asymmetry factor, the better the $\Delta d/d$ resolution. However, the dispersive spread of virtual sources due to the asymmetric diffraction by perfect crystals needs to be taken into account in order not to lose spatial resolution in the acquired images (Huang *et al.*, 2012; Hönnicke *et al.*, 2012).

In our setup, a collimator (as shown in Fig. 2*a*) was used to limit the horizontal divergence to $\Delta\theta_{\rm div} = 1.4 \times 10^{-3}$ rad. The source size is 0.4 mm (V) × 1.2 mm (H). Under these condi-

tions, the dimension of the horizontal beam cross section on the sample position is ∼1.5 mm. Since two different asymmetric diffraction planes were explored for the topography characterization, (31$\bar{4}$1) and (4$\bar{4}$02) with asymmetry factors b = −0.147 (diffraction angle θ = 37.17°, grazing-incidence angle = 8.15° and m = −1/b = 6.79) and b = −0.069 (diffraction angle θ = 44.72°, grazing-incidence angle = 3.97° and m = 14.5), respectively, the horizontal beam footprint on the sample was ∼10.6 mm (for 31$\bar{4}$1) and 21.7 mm (for 4$\bar{4}$02). Note that the spherical bent crystal will not be fully illuminated.

The 31$\bar{4}$1 reflection gives $\Delta\theta = 5.6 \times 10^{-5}$ rad and $\Delta d/d = 9.6 \times 10^{-5}$, and the 4$\bar{4}$02 reflection gives $\Delta\theta = 4.1 \times 10^{-5}$ rad and $\Delta d/d = 4.5 \times 10^{-5}$. Here, note that the asymmetry factor b is for the center of the spherical surface. Otherwise the asymmetry factor changes with the position since the incident angle is different for each different point on the spherical surface. Consequently, $\Delta\theta$ and $\Delta d/d$ also change from point to point on the surface.

In Fig. 2(b), it can be clearly seen from images (i)–(iii) that only part of the crystal diffracts (the horizontal dimensions of the topography images are smaller than the footprint dimensions described earlier in this section) since this is the acceptance limited by the line width of the Cu $K\beta$ X-ray emission line and the crystal is bent. Moreover, images (i) and (ii) of Fig. 2(b) show that each small crystal block diffracts nearly homogeneously [as expected from previous characterization (Hönnicke *et al.*, 2013)] except that there are some strains near the borders of the small crystal blocks. These strains indicate that the small crystal blocks are not completely independent of each other. As previously mentioned, the reason is that there remains a thin crystal layer that was not completely removed by the lapping/etching procedure. Finally, in Fig. 2(b), image (iii), the resolution of the quartz 4$\bar{4}$02 topography setup is only half of the previous 31$\bar{4}$1 topography setup. The contrast in image (iii) of Fig. 2(b) corresponds to surface imperfections rather than strong lattice misorientations. Otherwise, the misorientations should have also been shown in images (i)–(ii) of Fig. 2(b). In addition, structures due to the lapping/etching procedure can also be clearly seen in image (iii) of Fig. 2(b). These surface defects can be improved by a better final polishing of the quartz spherical analyzer crystal.

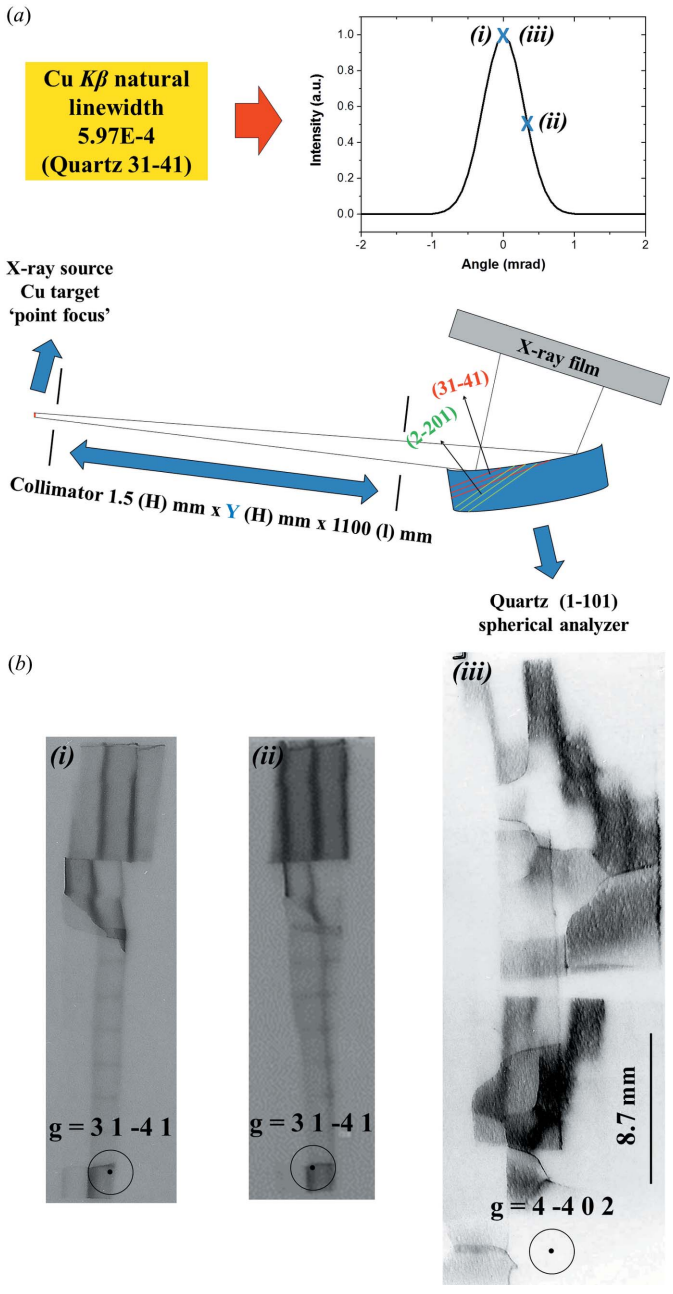

Figure 2
(a) Schematics of the experimental setup for the modified Berg–Barrett X-ray topography, based on asymmetric X-ray diffraction. Y is the size of the vertical slit which was set at 15 mm for quartz 31$\bar{4}$1 topography and 20 mm for quartz 4$\bar{4}$02 topography. (b) Topography of the quartz spherical analyzer crystal: (i) and (ii) taken for the 31$\bar{4}$1 asymmetric diffraction at different angular positions on the incoming natural Cu $K\beta$ emission line width, as shown in the top right inset; (iii) taken for the 4$\bar{4}$02 asymmetric diffraction at the top angular position on the incoming divergence.

3. XES experimental setup

The performance of the spherical quartz analyzer was tested by high-resolution XES of the Ni $K\alpha_{1,2}$ emission lines. Measurements were carried out at the X-ray Diffraction and Spectroscopy (XDS) beamline at the Laboratorio Nacional de

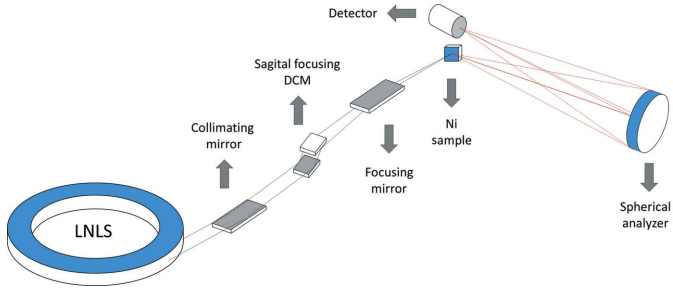

Figure 3
Schematic of the experimental setup at the XDS wiggler beamline at the LNLS. The Ni sample is set in the main axis of a six-circle Huber diffractometer and a one-dimensional detector is set in the main diffractometer arm, 1 m away from the quartz spherical analyzer crystal, for energy scans.

Luz Sincrotron (LNLS). XDS is a superconducting wiggler beamline. A schematic of the experimental setup is shown in Fig. 3. The quartz spherical analyzer was mounted in Rowland geometry on the main arm of a 5021 Huber diffractometer and positioned to collect fluorescence radiation emitted at 90° from the incidence direction in the horizontal plane. This measuring geometry allows reduction of the background radiation originated by scattered X-rays at the sample utilizing the polarization dependence of the scattering cross section. Sagittal alignment of the crystal was achieved by a stepping motor on the analyzer holder. The measuring geometry related to the sample orientation corresponds to the 45°–45° reflection geometry, commonly used in X-ray emission spectroscopy. He-filled sample–analyzer and analyzer–detector beam paths were used in order to further reduce the background intensity due to scattering in the air (as well as air absorption). Scintillation detectors were used to collect the analyzed fluorescence radiation and to monitor the intensity of the incident beam. The sample, analyzer and detector were aligned on a Rowland circle of 1 m diameter, in a Johann-type spectrometer. Radiation from a 3.5 T superconducting wiggler was monochromated to a bandwidth of 1.1 eV at the energy of the Ni *K* edge and horizontally focused to 2.7 mm by means of a sagittally bent double-crystal Si 111 monochromator. A cylindrically bent Rh mirror, located downstream of the monochromator, focuses the beam in the vertical direction to 0.46 mm. Energy scans of X-ray spectra emitted by a polycrystalline Ni foil were accomplished in the θ–2θ configuration in the vertical diffraction plane. The quartz $4\bar{4}04$ reflection was used to perform the energy analysis of the Ni $K\alpha_{1,2}$ X-rays. The corresponding Bragg angle of the analyzer at the energy of the Ni $K\alpha_1$ line was 82.64°. The analyzer Bragg angles were scanned in an angular range of about 4.7°, which spans an analyzed energy range of 72 eV around the $K\alpha$ emission lines.

The spectrometer resolution was determined by taking into account all geometrical effects according to Tirao *et al.* (2004), adapted to the present horizontal emission geometry. The different geometrical sources that contribute to the spectrometer resolution are listed in Table 1. The main contribution is provided by the crystal block size in the vertical (diffraction) plane. This contribution was reduced by putting a collimator (2 mm high in the diffraction plane) on the detector entrance window (see Table 1). The effective source size, caused by the penetration of the incident X-ray beam into the Ni sample (3.5 µm mean free path), contributes negligibly to the resolution. The intrinsic contribution of the crystal (width of the reflectivity curve), the contribution from misorientations of the crystal blocks and the contribution of the bent strains are negligible. The evaluated energy resolution at the $K\alpha_1$ line amounts to 1.07 eV, which is about half of its natural line width of 1.92 eV (Campbell & Papp, 2001). The dependence of the spectrometer resolution on the analyzed energy is displayed in Fig. 4. The energy of the incident X-ray beam was set to 67.45 eV above the *K* ionization threshold. The monochromator was calibrated by measuring the *K* absorption edge of Ni metal.

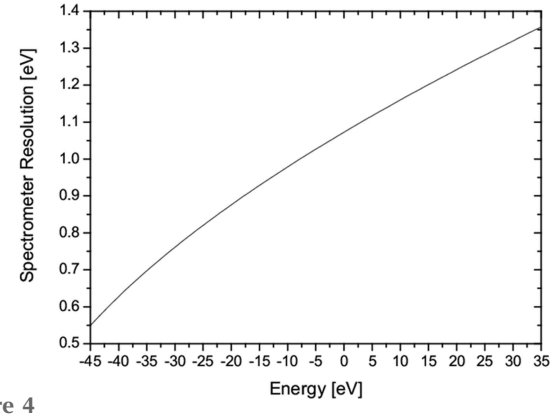

Figure 4
Spectrometer resolution as a function of the analyzed energy. The energy scale is relative to the energy of the Ni $K\alpha_1$ line energy.

Table 1
Individual geometrical contributions to the spectrometer energy resolution at the Ni $K\alpha_1$ energy.

The analyzer diffraction plane is the vertical plane.

	ΔE (eV)
Beam size (vertical)	0.45
Beam size (horizontal)	4.9×10^{-3}
Crystal block size (vertical)	1.40† (0.97)‡
Crystal block size (horizontal)	2.0×10^{-3}
Johann aberration	2.5×10^{-2}

† Without detector entrance collimator. ‡ With detector entrance collimator.

4. Data processing

Raw spectra were corrected for self-absorption in the sample and normalized to the monitor signal to account for fluctuations and for the long-term slow decay of the intensity of the incident beam. The absorption correction for an infinitely thick sample and symmetrical reflection geometry is given by $\mu_0 + \mu(E)$, where μ_0 and $\mu(E)$ are the attenuation coefficients at the incident and emitted energy, respectively. This correction is a decreasing function of the energy, which varies only 1.3% in the measured energy interval. Other correction factors, such as the scale factor $dE/d\theta \simeq 1/\sin(\theta)\tan(\theta)$, the crystal reflectivity $R_i \simeq \tan(\theta)$ and the analyzer solid angle $\Omega \simeq \sin(\theta)$, cancel each other regarding their functional dependency on the energy/Bragg angle. The experimental $K\alpha$ emission spectrum, after the data processing, is shown in Fig. 5. The energy-scale calibration was accomplished by setting the peak position of the $K\alpha_1$ line to the reference energy value given by Deslattes *et al.* (2003) and by using the absolute values of the lattice parameters of premium-grade α-quartz crystals reported by Brice (1985).

4.1. Fitting model. Physical grounds

It is well known that the $K\alpha$ and, to a larger extent, the $K\beta$ emission lines of 3*d* elements exhibit, in general, a noticeable asymmetry. High-resolution measurements along with Dirac–

Fock calculations showed that multiplet transitions with a 3*d* spectator hole, created by a shake-off process, are the main contribution to the satellite structure accompanying the *Kα* lines emitted from a Cu anode of an X-ray tube (Deutsch *et al.*, 1995). Ito *et al.* (2006) drew a similar conclusion for the Zn *Kα* spectrum, excited by the spectrum of an X-ray tube. In the case of a Ti target under the same excitation condition, contributions from $2p$ and $3d^2$ spectator hole satellites to the line shape of the *Kα* spectrum could also be seen (Lowe *et al.*, 2010).

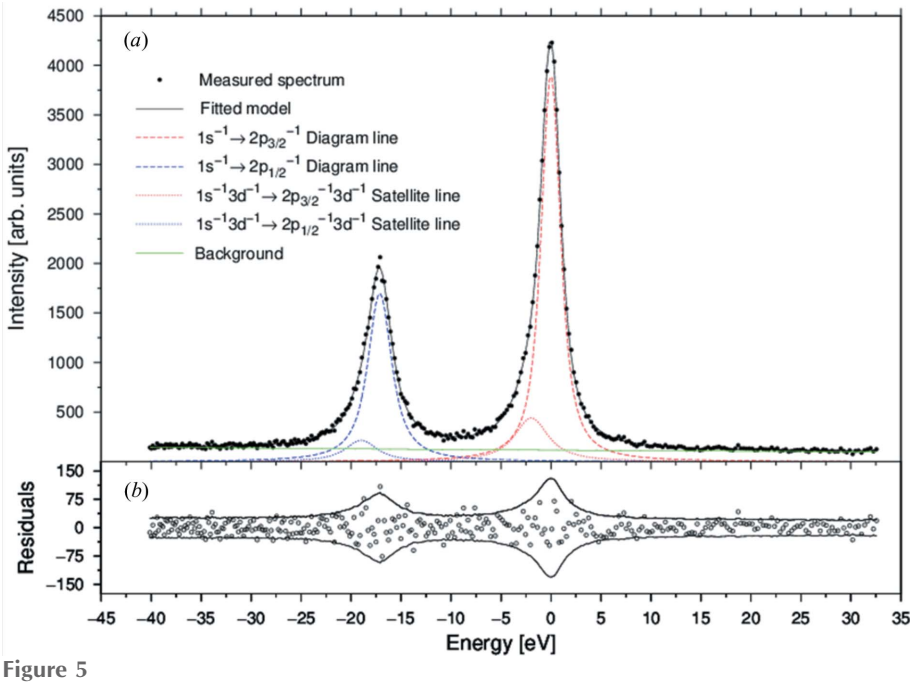

Figure 5
(*a*) Ni *Kα* X-ray emission spectrum measured at 67.45 eV above the *K*-shell ionization threshold (dots). Also shown are the total fit (solid line), individual fitting components represented by Lorentzian functions convoluted with the instrumental resolution function and the fitted background. (*b*) Fitting residuals. The solid lines denote $\pm 2\sigma$, where σ is the experimental standard uncertainty. The energy scale is relative to the maximum-intensity position of Ni $K\alpha_1$.

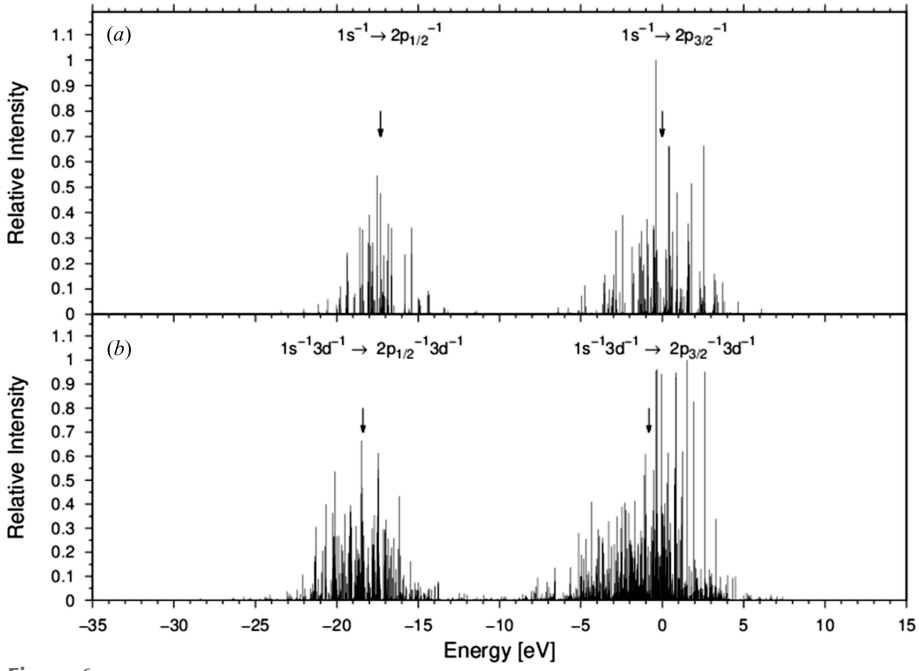

Figure 6
Stick diagrams for the transitions $1s^{-1} \rightarrow 2p^{-1}$ (*a*) and $1s^{-1}3d^{-1} \rightarrow 2p^{-1}3d^{-1}$ (*b*) in Ni, calculated with the *GRASP2K* code (Jönsson *et al.*, 2013). The strength of the transitions is represented by the height of the sticks. Stick heights are normalized to the strongest transition line of either the diagram or the satellite multiplets. The arrows indicate the position of the center of gravity for each multiplet. The energy scale is relative to the center of gravity of the $1s^{-1} \rightarrow 2p_{3/2}^{-1}$ multiplet.

Synchrotron radiation offers a unique possibility for selective excitation of a core level by using a sharply tuned and narrow-energy-bandwidth X-ray beam. Consequently, line-shape studies can be undertaken by suppressing the contributions of some satellite structures. As mentioned earlier, in our measurements, the energy of the incident beam was set to 67.45 eV above the *K* absorption threshold, such that $1s^{-1}3p^{-1}$ shake processes are not excited. This is due to the thresholds that are at 75.1 and 77.3 eV above the *K*-edge energy for $1s^{-1}3p_{3/2}{}^{-1}$ and $1s^{-1}$-$3p_{1/2}{}^{-1}$ excitations, respectively (where nl_j^{-1} denotes a vacancy in the nl_j atomic level). Here, the threshold values were computed using the $Z + 1$ model and the binding energies compiled by Fuggle & Mårtensson (1980). Hence, the experimental *Kα* emission spectrum contamination by $3p$ spectator hole satellites can be suppressed.

On the other hand, as 3*d* electrons form part of the conduction band in a solid target, $1s^{-1}3d^{-1}$ shake processes can be excited by any X-ray photon energies higher than the *K*-shell ionization threshold. Consequently, 3*d* spectator hole satellites should always be present in the emission spectrum of a 3*d* metal. In order to address this issue, the diagram lines ($1s^{-1} \rightarrow 2p^{-1}$ transitions) and the multiplet structure due to a 3*d* spectator hole ($1s^{-1}3d^{-1} \rightarrow 2p^{-1}3d^{-1}$ transitions) were simulated using the *GRASP2K* code (Jönsson *et al.*, 2013). Calculated transitions for Ni are shown as stick diagrams in Fig. 6, where the atomic ground-state configuration of Ni ($[\mathrm{Ar}]3d^8 4s^2$) was assumed. As shown in Fig. 6, the distribution of multiplet lines for diagram transitions is quite symmetric, which can also be seen for Ti calculation (Lowe *et al.*, 2010). The simulated satellite multiplets also show a nearly symmetrical distribution, but the center of gravity is shifted to a

lower energy by 0.82 eV (1.08 eV) with respect to the $1s^{-1}\rightarrow 2p_{3/2}{}^{-1}$ ($1s^{-1}\rightarrow 2p_{1/2}{}^{-1}$) diagram line. As a consequence, since the separation between the centers of gravity of the diagram and the satellite multiplet lines is smaller than the natural line width, a skewed line shape to lower energies is expected for the $K\alpha_1$ and the $K\alpha_2$ emission lines. Note that here it is beyond the scope of this work to obtain precise theoretical values for the emission line strengths and energies for the $K\alpha_{1,2}$ lines or to provide an accurate theoretical description of the shape of the $K\alpha$ spectrum. Such theoretical studies would require much more refined and time-consuming computations, similar to those performed for Cu (Chantler *et al.*, 2009, 2010, 2012) and Ti (Lowe *et al.*, 2010; Chantler *et al.*, 2013). The purpose of the present simulations is only to suggest and support a phenomenological model for the spectral shape of the Ni $K\alpha_{1,2}$ spectrum, which will be used to fit the experimental data. On the basis of these results, a phenomenological representation for the multiplets of the diagram line and the $1s^{-1}3d^{-1}$ satellite structure by two Lorentzian functions was assumed for each $K\alpha$ emission line. A similar analytical representation, based also on a physical origin, was proposed for the $K\alpha$ lines of Cu (Härtwig *et al.*, 1993; Ito *et al.*, 2006) and Zn (Ito *et al.*, 2006). Hölzer *et al.* (1997) used a series of Lorentzian functions to describe the line shape of emission spectra for several 3*d* transition metals, but without attempting to make a physical interpretation of probable satellite contributions to the emission lines. In that work, the number of fitted Lorentzian functions was determined from a convergence criterion and depended on the element.

Exchange interactions between electrons of the partially occupied 3*d* shell of some transition metals and one electron of the 1*s* shell (with a hole created by photoionization in the initial state), or between unpaired 3*d* electrons and electrons of the *lp* shell (with a hole created by the electronic transition $lp\rightarrow 1s$ in the final state), give rise to complex multiplet structures in the emission lines. This can be clearly seen in Fig. 6. In some cases, the multiplet splitting could produce an additional broadening of the emission lines beyond the lifetime width as well as an asymmetric line shape. This effect is more remarkable in the $K\beta_{1,3}$ emission spectrum because of the strong exchange interactions between 3*p* and 3*d* electrons (Tsutsumi *et al.*, 1976). For compounds of transition metals, charge transfer effects can also play a fundamental role in the shape of the $K\beta_{1,3}$ emission line (Kawai *et al.*, 1990). Our present simulations show a quite symmetrical multiplet distribution, which indicates that exchange interactions are not a source of noticeable asymmetry for the $K\alpha_{1,2}$ lines of Ni.

Another contributing process for distortion of the emission line spectral shape in transition metals is the radiative Auger (RA) transition that involves Auger electrons from the 3*d* level. As 3*d* electrons are weakly bound in transition metal atoms, those RA processes have their onset very close to the energy of the associated X-ray emission line. In the case of Ni, the peak maximum of the principal component of the $KL_2M_{4,5}$ and $KL_3M_{4,5}$ RA transitions would be located at 4.13 and 3.65 eV towards lower energies from the $K\alpha_2$ and $K\alpha_1$ line positions, respectively, as expected from the Ni *KLM* Auger transition energies (Egri *et al.*, 2008). From experimental *KLM* Auger intensities (Egri *et al.*, 2008) and from the multivacancy-state production and emission rates calculated by Scofield (1974), the rate of the $KL_3M_{4,5}$ ($KL_2M_{4,5}$) RA transition relative to the rate of the $1s^{-1}\rightarrow 2p_{3/2}{}^{-1}$ ($1s^{-1}\rightarrow 2p_{1/2}{}^{-1}$) X-ray transition in Ni is estimated to be as low as 2.9×10^{-4} (3.0×10^{-4}). The relative intensity of $KL_3M_{4,5}$ RA transitions in Cu was estimated to be of a similar magnitude (5×10^{-4}) (Maskil & Deutsch, 1988). Thus, it is expected that the spectral weight of such RA transitions is negligible in relation to the $K\alpha_{1,2}$ spectral intensity. Indeed, an experimental and theoretical study of the *K* X-ray spectrum of Mn showed no evidence of *KLM* RA satellites (Jonnard *et al.*, 2002). By contrast, RA transitions of the type $KM_{4,5}M_{4,5}$ can distort the $K\beta_5$ emission line on its low-energy tail as observed in high-resolution studies in Cu (Enkisch *et al.*, 2004). The weak *KLN* Auger transitions could not be resolved in the high-resolution Auger spectra measured by Egri *et al.* (2008). The relative rate of $KL_{2,3}N_1$ RA to $K\alpha_{1,2}$ transitions is expected to be at least one order of magnitude lower than that for $KL_{2,3}M_{4,5}$ RA transitions (Scofield, 1974). The onsets of other, mostly much stronger RA transitions of the *KLM* group are, at least, 54 eV (to the lower energies) from the onset of the $KL_2M_{4,5}$ transition (Egri *et al.*, 2008). This energy is too far from the $K\alpha_{1,2}$ lines to distort them. In addition, those RA satellites are outside the measured energy range.

Each spectral component of the $K\alpha_{1,2}$ emission spectrum is analytically represented by the Lorentzian profile

$$\mathrm{L}(E) = \frac{A}{1+(E-E_0)^2/w^2}, \qquad (1)$$

where the fitting parameters A, E_0 and w are, respectively, the amplitude, the position and the width (it measures the half-width at half-maximum, HWHM) of the profile. To take into account the instrumental broadening effects, the Lorentzian peaks are convolved by a Gaussian-shaped instrumental response function. Then, the whole model to fit the corrected measured emission spectrum is given by

$$\mathrm{M}(E) = \sum_{i=1}^{4} \int_{-\infty}^{+\infty} \mathrm{L}_i(E')\mathrm{G}(E-E')\,\mathrm{d}E' + \mathrm{B}(E), \qquad (2)$$

where $\mathrm{G}(E-E')$ is the unity-area Gaussian profile, given by the equation

$$\mathrm{G}(E-E') = \frac{2[\ln(2)]^{1/2}}{\pi^{1/2}\Delta(E')}\exp\left[-\frac{4\ln(2)}{\Delta^2(E')}(E-E')^2\right], \qquad (3)$$

and $\Delta(E')$ (the FWHM of the Gaussian profile) is the energy-dependent instrumental resolution given in Fig. 4. The background $\mathrm{B}(E)$ was simulated by a second-order polynomial function with all three parameters free to vary during the fitting process. A detailed study of the energy dependence of the scattered radiation contributing to the background in XES using a Johann-type spectrometer will be given elsewhere (Paredes Mellone *et al.*, in preparation). We found that in the present measurements a nonlinear component must be

Table 2
Fitting parameters of the Lorentzian profiles representing each spectral component.

	$1s^{-1}\rightarrow 2p_{3/2}{}^{-1}$	$1s^{-1}3d^{-1}\rightarrow 2p_{3/2}{}^{-1}3d^{-1}$	$1s^{-1}\rightarrow 2p_{1/2}{}^{-1}$	$1s^{-1}3d^{-1}\rightarrow 2p_{1/2}{}^{-1}3d^{-1}$
E (eV)	−0.011 (15)	−2.0 (2)	−17.12 (4)	−19.0 (4)
w (eV)	0.91 (2)	1.9 (1)	1.28 (4)	1.8 (2)
A ($\times 10^3$)	4.64 (6)	0.46 (7)	1.83 (7)	0.23 (8)
$\chi^2_{\rm reduced}$		1.418		

considered for an accurate description of the background. A least-squares fitting of the model given by equation (2) to the experimental data was performed with the *MINPACK* code (Moré *et al.*, 1980). As the goodness-of-fit parameter, the weighted sum of residuals (χ^2) was minimized, where the weights are the inverse of the squared experimental uncertainties. Considering that a precise determination of the background is critical whenever there are weak satellite peaks present, the analytical models for the peaks and the background were fitted separately. In accordance with Bevington & Robinson (2003), the following fitting procedure steps were adopted: (i) only the background curve is fitted outside the region of the peaks to obtain an initial estimate of its parameters; (ii) the analytical model given in equation (2) is fitted to the central region with background parameters fixed to the values obtained in the first step; (iii) the background curve is fitted to the outside region as in the first step, but now including contributions of the tails of the Lorentzian profiles with parameters fixed to the values obtained in the second step. Then, the fitting process is repeated from the second step, with background parameters updated, until convergence is achieved. The convergence criterion was set to achieve a change in χ^2 (between two consecutive iterations) smaller than 1%. Four fitting cycles were needed in order to achieve the convergence limit. Special care was taken to provide enough data to fit the background with our present procedure, *i.e.* the emission spectra were measured in a sufficiently wide energy range. The value of the reduced χ^2 (Table 2) was computed in the entire fitting region, so that it measures the accuracy of the fitting model both for the background and for the peak functions.

5. Results and discussion

Our fitting results are shown in Fig. 5 with the fitting parameters listed in Table 2. The small and non-systematic residuals show the high fitting quality and demonstrate that two Lorentzian functions, convolved with a Gaussian-shaped instrumental response function, are adequate to describe each Ni $K\alpha$ emission line. Most residuals lie within the $\pm 2\sigma$ range, where the experimental uncertainty (σ) arises from the counting statistics propagated through the data processing. The main Lorentzian peaks describe the diagram line, while the secondary peaks represent the $1s^{-1}3d^{-1}\rightarrow 2p^{-1}3d^{-1}$ satellite transitions. In the work by Hölzer *et al.* (1997), the $K\alpha_1$ line was also represented by two Lorentzian functions, but a weak contribution from a third Lorentzian was necessary to describe the $K\alpha_2$ line. A precise theoretical study of the $K\alpha_{1,2}$ lines of Ti (Lowe *et al.*, 2010) predicted a weak $3d^2$ spectator hole satellite. This satellite peak would display an amplitude as low as 2σ and would be located at lower energies with respect to the $3d$ spectator hole satellite. Nevertheless, such a satellite contribution was not included in a later theoretical study (Chantler *et al.*, 2013). The third weak Lorentzian peak phenomenologically included in the fitting model for the $K\alpha_2$ line of Ni in the work of Hölzer *et al.* (1997) might be a sign of $1s^{-1}3d^{-2}$ excitation processes. In terms of the radiative Auger processes, structures arising from *KLM* RA transitions cannot be resolved in our experimental $K\alpha_{1,2}$ emission spectrum. This is expected because of their very low relative intensity. Likewise, no RA satellite was observed in the $K\alpha_{1,2}$ emission spectrum of Mn (Jonnard *et al.*, 2002). Within the experimental uncertainties, our present measurements exhibit no satellite contributions other than that from $3d$ spectator hole multiplets.

5.1. Diagram lines

The energy separation between the main Lorentzian peaks of the $K\alpha_1$ and $K\alpha_2$ lines is 17.11 ± 0.04 eV, which is in good agreement with the results of Hölzer *et al.* (1997) of 17.15 eV. It should be pointed out that, owing to the variability of the absolute value of the lattice parameter of premium-grade α-quartz crystals (Brice, 1985), a variation of the $K\alpha_1$–$K\alpha_2$ energy separation over the range from 17.06 to 17.21 eV might be expected.

The shape of the emission lines is characterized by its width and its index of asymmetry. The measured widths of the diagram lines (FWHM) are 1.82 ± 0.05 eV ($K\alpha_1$) and 2.56 ± 0.08 eV ($K\alpha_2$), which are in close agreement with the experimental values of Ito *et al.* (2006) and with the values obtained from the recommended widths of atomic levels of 1.92 eV ($K\alpha_1$) and 2.37 eV ($K\alpha_2$) (Campbell & Papp, 2001). The observed FWHM of the $K\alpha_2$ diagram line is noticeably larger than that of the $K\alpha_1$ diagram line, which is in agreement with the general tendency among experimental values [see *e.g.* Fig. 2 of Hölzer *et al.* (1997)]. X-ray photoemission spectroscopy (XPS) results (Fuggle & Alvarado, 1980) suggest that Coster–Kronig transitions, of the type $L_2L_3M_{4,5}$, should be responsible for the reduction of the lifetime of an L_2 vacancy with respect to one in the L_3 subshell. Note that these Coster–Kronig transitions for some transition metal elements could be energetically forbidden in a free-atom model but allowed in the solid-state model (Yin *et al.*, 1973). Assuming that the Auger and radiative widths are almost the same for the L_2 and L_3 levels (McGuire, 1971), the difference between $K\alpha_2$ and $K\alpha_1$ line widths can measure the contribution of Coster–Kronig transitions to the L_2 level width. Our measured difference between $K\alpha_1$ and $K\alpha_2$ line widths is 0.74 ± 0.09 eV, which is very close to the $L_2L_3M_{4,5}$ Coster–Kronig width evaluated by Yin *et al.* (1973) of 0.801 eV. In agreement with

early XPS studies, our results indicate that the reduced lifetime of the L_2 level can be accounted for by $L_2L_3M_{4,5}$ Coster–Kronig transitions. Line widths for the whole emission peaks, *i.e.* including satellites, of 2.24 and 3.16 eV were reported for the $K\alpha_1$ and $K\alpha_2$ lines, respectively (Hölzer *et al.*, 1997). The remarkable discrepancy relative to our present widths indicates the extent to which satellites can distort the line shape. At this point, it is worth pointing out that charged particles as an ionizing probe of atomic inner shells do not allow one to control the excitation of multiple vacancies (both due to shake processes and due to double ionization produced by the incident particles). Besides a probable lack of accuracy in the correction for instrumental broadening, the excitation condition could be a cause of the considerable dispersion observed in the reported line widths. On the other hand, *K*-shell ionization produced by photoabsorption using a monochromatic but tunable X-ray beam becomes possible for avoiding the contribution of some satellites and, hence, for measuring a clean emission spectrum.

The index of asymmetry is defined as the ratio between the HWHM of the low-energy side of the peak emission line and the HWHM of the high-energy side of the peak emission line. This index was obtained from the reconstructed emission profile, which includes both spectral components (the main diagram line and the satellite line) for each $K\alpha$ peak. The values obtained here were 1.08 ± 0.07 and 1.16 ± 0.09 for the $K\alpha_1$ and $K\alpha_2$ emission profiles, respectively. The uncertainty values were calculated from the propagation of the uncertainties of the fit parameters onto the HWHM of the reconstructed emission profile. Measurements by Hölzer *et al.* (1997) yield values of 1.18 ± 0.05 ($K\alpha_1$) and 1.21 ± 0.07 ($K\alpha_2$). Both results indicate that the $K\alpha_2$ emission peak is slightly more asymmetric, but this tendency is not conclusive if the experimental uncertainties are considered.

According to our simulations (Fig. 6), the secondary peak of each emission line in the experimental spectrum can be exclusively assigned to the satellite peak associated with 3*d* spectator hole transitions instead of an asymmetry arising from the multiplet splitting of the diagram transitions. Consequently, the intensity partitioning between the different spectral components (the diagram and satellite lines) should not be a serious problem in the case of Ni as it is for other transition metals (Hölzer *et al.*, 1997). Owing to the normalization of the Lorentzian functions used in the fitting model, the integrated intensity for each peak can be directly computed from the fitted parameters according to $I = \pi A w$. The present $K\alpha_2$–$K\alpha_1$ intensity ratio of 0.54 ± 0.04 is in fairly good agreement with the value of 0.52 ± 0.02 reported by Hölzer *et al.* (1997). The measured intensity ratio for the main diagram lines, *i.e.* excluding satellite lines, is 0.55 ± 0.03. The similarity between the two values indicates that the contamination of each $K\alpha$ peak by satellite intensities would be nearly equal in Ni.

5.2. Satellite lines

As discussed above, the satellite structure accompanying the $1s^{-1} \rightarrow 2p^{-1}$ transition lines on their low-energy side can be ascribed to the $1s^{-1}3d^{-1} \rightarrow 2p^{-1}3d^{-1}$ transitions, where the 3*d* hole was produced by the shake processes. In the present work, the satellite lines were found to be located at 2.0 ± 0.2 eV (the $2p_{3/2}$ spectator hole) and at 1.9 ± 0.4 eV (the $2p_{1/2}$ spectator hole) towards lower energies from the positions of the $K\alpha_1$ and $K\alpha_2$ diagram lines, respectively. These values are about 1 eV further shifted to lower energies when compared to the center of gravity of the simulated satellite multiplets. A more refined calculation model would be required to attempt a more accurate theoretical description of the individual spectral components of the emission spectrum. The secondary Lorentzian fitted by Hölzer *et al.* (1997) to the $K\alpha_1$ line is located at 1.75 eV from the main peak, in close agreement with our measurements. To describe the line shape of the $K\alpha_2$ line, the model from Hölzer *et al.* (1997) utilizes two Lorentzians displaced by 1.26 and 3.1 eV from the main peak. Instead, in our case, it is a single Lorentzian shifted by 1.9 eV, about midway between the two Lorentzian functions of that work.

Unlike the diagram lines, both satellites have very similar widths of 3.8 ± 0.2 eV ($2p_{3/2}$ spectator hole) and 3.6 ± 0.4 eV ($2p_{1/2}$ spectator hole), which could suggest that the broadening of the satellites would be dominated by the wide energy range where the multiplet splitting of the $1s^{-1}3d^{-1} \rightarrow 2p^{-1}3d^{-1}$ transition spreads.

The probability of an electron being excited to an unoccupied bound state (the shake-up process) or ejected into a state of the continuum energy spectrum (the shake-off process) upon creating an inner shell vacancy was calculated in the sudden approximation (Mukoyama & Taniguchi, 1987; Kochur *et al.*, 2002; Lowe *et al.*, 2911). Assuming that the radiative transition rate for filling an inner shell vacancy is not significantly altered by the presence of a spectator hole in an outer shell, the experimental total shake (shake-up and shake-off) probability can be computed from the intensity ratio between the satellite and diagram lines. Our present results are $21 \pm 3\%$ and $18 \pm 7\%$ for the $2p_{3/2}{}^{-1}3d^{-1}$ and the $2p_{1/2}{}^{-1}$-$3d^{-1}$ satellites, respectively. These values are in agreement with the satellite intensity measured by Ito *et al.* (2006) of about 21.4%. In that work, the authors reported a single value, which was computed from the combined intensity of both satellites and diagram lines.

Ab initio calculations of the probability of excitation of a 3*d* electron as a result of a sudden 1*s* vacancy production have been performed by several authors using different theoretical approaches. Earlier calculations based on single-configuration wavefunctions predicted appreciably low values [9.742% (Mukoyama & Taniguchi, 1987) and 10.4% (Kochur *et al.*, 2002)]. The calculated probability from a multi-configuration atomic model of 22% [taken from Fig. 1 of Lowe *et al.* (2011)] agrees very well with our experimental results. These results demonstrate the importance of including multi-configurational effects in open shell atoms for atomic structure calculations. It should be mentioned that Lowe *et al.* (2011) have considered all possible distributions of electrons among the 3*d* and 4*s* shells and the computed shake probabilities were averaged over all valence-state configurations. In later work

(Chantler *et al.*, 2013), individual shake probabilities for each isolated configuration were computed. Calculations accounting for up to $n = 5$ correlations in generating the configuration state function basis provided shake probabilities in close agreement with our results, both for the nominal $3d^8 4s^2$ valence configuration and for the $3d^{10}$ configuration. Nevertheless, depending on the level of correlation used, theoretical results for the $3d^8 4s^2$ configuration show important variations in the calculated shake probabilities. Precise simulations of the Ni emission spectra would be useful to check if an admixture of valence states should be considered to reconstruct the emission spectrum, similar to what has been done for Cu (Chantler *et al.*, 2012).

6. Conclusions

An α-quartz $4\bar{4}04$ spherical analyzer crystal was constructed for use in high-energy-resolution X-ray emission spectroscopy. The misorientation of the crystal blocks on the concave spherical surface was characterized by a topographic study and misorientation values of $\sim 10^{-5}$ rad were determined. The contribution of the misorientation to the spectrometer resolution is two orders of magnitude smaller than the angular divergences introduced by the geometrical effects. The quartz analyzer demonstrated its successful applications and capabilities in the high-resolution analysis of the Ni $K\alpha$ emission spectrum with the $4\bar{4}04$ reflection. For this experiment, an analytical representation of each $K\alpha$ line by two Lorentzian functions provides a fit of good quality for the emission spectrum of Ni. By a proper choice of the excitation energy to preclude satellites arising from $3p$ spectator hole transitions and by modeling each $1s^{-1}3d^{-1}$ satellite multiplet with a single Lorentzian profile, we demonstrated that it is possible to study the tiny spectral features of the individual components. The simulation of the multiplet splitting of the diagram and satellite emission lines, based on a multi-configurational atomic scheme, is of fundamental importance for proposing an appropriate analytical representation of the emission profile. An accurate evaluation of the energy-dependent instrumental broadening is required in order to have reliable values for the line width and index of asymmetry of the emission lines. The origin of the observed asymmetry of the $K\alpha_{1,2}$ lines was assigned to satellite structures due to $3d$ spectator hole transitions on the low-energy side of the diagram lines. No satellite contribution due to radiative Auger transitions could be detected in the measured spectrum concerning the experimental uncertainty. The measured $1s^{-1}3d^{-1}$ satellite intensity supports a multi-configuration framework for shake probability calculations.

Acknowledgements

The authors acknowledge LNLS/CNPEM/MCT for beamtime (under proposal XRD2-10886/2013). MGH and CC gratefully acknowledge CNPq/PQ (309109/2013-2 and 309614/2013-9) for their research fellowships. XRH and YQC are supported by the US Department of Energy, Office of Science, Office of Basic Energy Sciences, under contract Nos. DE-AC02-06CH11357 and DE-SC0012704, respectively. Financial support from SeCyT (Universidad Nacional de Córdoba, Argentina) and CONICET (Argentina) is gratefully acknowledged. LMB is a fellow of CONICET.

References

Authier, A. (2001). *Dynamical Theory of X-ray Diffraction*, ch. 17. Oxford University Press.
Barrett, C. (1945). *Trans. Met. Soc. AIME*, **161**, 15–64.
Barrett, R., Baruchel, J., Härtwig, J. & Zontone, F. (1995). *J. Phys. D Appl. Phys.* **28**, A250–A255.
Berg, W. (1931). *Naturwissenschaften*, **19**, 391–396.
Bevington, P. & Robinson, D. (2003). *Data Reduction and Error Analysis for the Physical Sciences.* New York: McGraw Hill.
Bond, W. L. & Andrus, J. (1952). *Am. Mineral.* **37**, 622–632.
Brice, J. C. (1985). *Rev. Mod. Phys.* **57**, 105–146.
Cai, Y. Q. (2004). *AIP Conf. Proc.* pp. 340–343.
Campbell, J. J. & Papp, T. (2001). *At. Data Nucl. Data Tables*, **77**, 1–56.
Chantler, C. T., Hayward, A. C. L. & Grant, I. P. (2009). *Phys. Rev. Lett.* **103**, 123002.
Chantler, C. T., Lowe, A. & Grant, I. P. (2010). *Phys. Rev. A*, **82**, 052505.
Chantler, C. T., Lowe, A. & Grant, I. P. (2012). *Phys. Rev. A*, **85**, 032513.
Chantler, C. T., Lowe, A. & Grant, I. P. (2013). *J. Phys. B At. Mol. Opt. Phys.* **46**, 015002.
Culity, B. D. & Stock, S. R. (2014). *Elements of X-ray diffraction*, 3rd ed. Upper Saddle River: Pearson.
Deslattes, R. D., Kessler, E. G. Jr, Indelicato, P., de Billy, L., Lindroth, E. & Anton, J. (2003). *Rev. Mod. Phys.* **75**, 35–99.
Deutsch, M., Hölzer, G., Härtwig, J., Wolf, J., Fritsch, M. & Förster, E. (1995). *Phys. Rev. A*, **51**, 283–296.
Dudley, M., Wang, S. P., Huang, W., Carter, C. H., Tsvetkov, V. F. & Fazi, C. (1995). *J. Phys. D Appl. Phys.* **28**, A63–A68.
DuMond, J. W. M. (1937). *Phys. Rev.* **52**, 872–883.
Egri, S., Kövér, L., Drube, W., Cserny, I. & Novák, M. (2008). *J. Electron Spectrosc. Relat. Phenom.* **162**, 115–121.
Enkisch, H., Sternemann, C., Paulus, M., Volmer, M. & Schülke, W. (2004). *Phys. Rev. A*, **70**, 022508.
Fister, T. T., Seidler, G. T., Wharton, L., Battle, A. R., Ellis, T. B., Cross, J. O., Macrander, A. T., Elam, W. T., Tyson, T. A. & Qian, Q. (2006). *Rev. Sci. Instrum.* **77**, 063901.
Fuggle, J. C. & Alvarado, S. F. (1980). *Phys. Rev. A*, **22**, 1615–1624.
Fuggle, J. C. & Mårtensson, N. (1980). *J. Electron Spectrosc. Relat. Phenom.* **21**, 275–281.
Gog, T., Casa, D. M., Said, A. H., Upton, M. H., Kim, J., Kuzmenko, I., Huang, X. & Khachatryan, R. (2013). *J. Synchrotron Rad.* **20**, 74–79.
Härtwig, J. (1999). *X-ray Diffraction Imaging (X-ray Topography). An Overview of Techniques and Applications*, http://www.esrf.eu/UsersAndScience/Experiments/Imaging/ID19/Techniques/Diffraction/Overview.
Härtwig, J., Hölzer, G., Wolf, J. & Förster, E. (1993). *J. Appl. Cryst.* **26**, 539–548.
Hill, J. P., Coburn, D. S., Kim, Y.-J., Gog, T., Casa, D. M., Kodituwakku, C. N. & Sinn, H. (2007). *J. Synchrotron Rad.* **14**, 361–365.
Hölzer, G., Fritsch, M., Deutsch, M., Härtwig, J. & Förster, E. (1997). *Phys. Rev. A*, **56**, 4554–4568.
Hönnicke, M. G., Huang, X., Cusatis, C., Koditwuakku, C. N. & Cai, Y. Q. (2013). *J. Appl. Cryst.* **46**, 939–944.
Hönnicke, M. G., Manica, J., Mazzaro, I., Cusatis, C. & Huang, X.-R. (2012). *Rev. Sci. Instrum.* **83**, 113702.

Huang, X. R., Macrander, A. T., Honnicke, M. G., Cai, Y. Q. & Fernandez, P. (2012). *J. Appl. Cryst.* **45**, 255–262.
Ishikawa, D., Ellis, D. S., Uchiyama, H. & Baron, A. Q. R. (2015). *J. Synchrotron Rad.* **22**, 3–9.
Ito, Y., Tochio, T., Oohashi, H. & Vlaicu, A. M. (2006). *Radiat. Phys. Chem.* **75**, 1534–1537.
Jonnard, P., Giorgi, G. & Bonnelle, C. (2002). *Phys. Rev. A*, **65**, 032507.
Jönsson, P., Gaigalas, G., Bieroń, J., Fischer, C. F. & Grant, I. P. (2013). *Comput. Phys. Commun.* **184**, 2197–2203.
Kawai, J., Takami, M. & Satoko, C. (1990). *Phys. Rev. A*, **65**, 2193–2196.
Ketenoglu, D., Harder, M., Klementiev, K., Upton, M., Taherkhani, M., Spiwek, M., Dill, F.-U., Wille, H.-C. & Yavaş, H. (2015). *J. Synchrotron Rad.* **22**, 961–967.
Kochur, A. G., Dudenko, A. I. & Petrini, D. (2002). *J. Phys. B At. Mol. Opt. Phys.* **35**, 395–399.
Lang, A. R. (1959). *Acta Cryst.* **12**, 249–250.
Lowe, J. A., Chantler, C. T. & Grant, I. P. (2010). *Phys. Lett. A*, **374**, 4756–4760.
Lowe, J. A., Chantler, C. T. & Grant, I. P. (2011). *Phys. Rev. A*, **83**, 060501.
Lübbert, D., Baumbach, T., Härtwig, J., Boller, E. & Pernot, E. (2000). *Nucl. Instrum. Methods Phys. Res. Sect. B*, **160**, 521–527.
Lübbert, D., Ferrari, C., Mikulík, P., Pernot, P., Helfen, L., Verdi, N., Korytár, D. & Baumbach, T. (2005). *J. Appl. Cryst.* **38**, 91–96.
Maskil, N. & Deutsch, M. (1988). *Phys. Rev. A*, **38**, 3467–3472.
McGuire, E. J. (1971). *Phys. Rev. A*, **3**, 587–594.
Moré, J. J., Garbow, B. S. & Hillstrom, K. E. (1980). *User Guide for MINPACK-1*. Argonne National Laboratory Report ANL-80-74, Argonne, IL, USA.
Mortensen, D. R., Seidler, G. T., Bradley, J. A., Lipp, M. J., Evans, W. J., Chow, P., Xiao, Y.-M., Boman, G. & Bowden, M. E. (2013). *Rev. Sci. Instrum.* **84**, 083908.
Mukoyama, T. & Taniguchi, K. (1987). *Phys. Rev. A*, **36**, 693–698.
Palmeri, P., Quinet, P., Mendoza, C., Bautista, M. A., García, J., Witthoeft, M. C. & Kallman, T. R. (2008). *ApJS*, **179**, 542–552.
Pinsker, Z. G. (1978). *Dynamical Scattering of X-rays in Crystals.* Berlin: Springer-Verlag.
Ramachandran, G. N. (1944). *Proc. Indian Acad. Sci. A*, **19**, 280–292.
Schülke, W. (1991). *Handbook on Synchrotron Radiation*, edited by G. Brown & D. E. Moncton, Vol. 3, ch. 15, pp. 565–637. Amsterdam: Elsevier Science Publishers.
Schülke, W. & Nagasawa, H. (1984). *Nucl. Instrum. Methods Phys. Res.* **222**, 203–206.
Scofield, J. H. (1974). *Phys. Rev. A*, **9**, 1041–1049.
Sergueev, I., Wille, H.-C., Hermann, R. P., Bessas, D., Shvyd'ko, Y. V., Zając, M. & Rüffer, R. (2011). *J. Synchrotron Rad.* **18**, 802–810.
Sinars, D. B., Bennett, G. R., Wenger, D. F., Cuneo, M. E. & Porter, J. L. (2003). *Appl. Opt.* **42**, 4059–4071.
Sokaras, D., Weng, T.-C., Nordlund, D., Alonso-Mori, R., Velikov, P., Wenger, D., Garachtchenko, A., George, M., Borzenets, V., Johnson, B., Rabedeau, T. & Bergmann, U. (2013). *Rev. Sci. Instrum.* **84**, 053102.
Sutter, J. P., Baron, A. Q. R., Ishikawa, T. & Yamazaki, H. (2005). *J. Phys. Chem. Solids*, **66**, 2306–2309.
Sutter, J. P., Baron, A. Q. R., Miwa, D., Nishino, Y., Tamasaku, K. & Ishikawa, T. (2006). *J. Synchrotron Rad.* **13**, 278–280.
Tanner, B. K. (1976). *X-ray Diffraction Topography*, pp. 24–25. Oxford: Pergamon.
Tirao, G., Stutz, G. & Cusatis, C. (2004). *J. Synchrotron Rad.* **11**, 335–342.
Torres Deluigi, M., de Groot, F. M. F., López-Díaz, G., Tirao, G., Stutz, G. & Riveros de la Vega, J. (2014). *J. Phys. Chem. C*, **118**, 22202–22210.
Tsutsumi, K., Nakamori, H. & Ichikawa, K. (1976). *Phys. Rev. B*, **13**, 929–933.
Tuomi, T., Naukkarinen, K. & Rabe, P. (1974). *Phys. Status Solidi A*, **25**, 93–106.
Verbeni, R., Kocsis, M., Huotari, S., Krisch, M., Monaco, G., Sette, F. & Vanko, G. (2005). *J. Phys. Chem. Solids*, **66**, 2299–2305.
Verbeni, R., Pylkkänen, T., Huotari, S., Simonelli, L., Vankó, G., Martel, K., Henriquet, C. & Monaco, G. (2009). *J. Synchrotron Rad.* **16**, 469–476.
Yavaş, H., Ercan Alp, E., Sinn, H., Alatas, A., Said, A., Shvyd'ko, Y., Toellner, T., Khachatryan, R., Billinge, S., Zahid Hasan, M. & Sturhahn, W. (2007). *Nucl. Instrum. Methods Phys. Res. Sect. A*, **582**, 149–151.
Yin, L. I., Adler, I., Chen, M. H. & Crasemann, B. (1973). *Phys. Rev. A*, **7**, 897–903.